Effects of explicit atmospheric convection at high CO_2

Nathan P. Arnold[a,1,2], Mark Branson[b], Melissa A. Burt[b], Dorian S. Abbot[c], Zhiming Kuang[a,d], David A. Randall[b,2], and Eli Tziperman[a,d,2]

[a]Department of Earth and Planetary Sciences, Harvard University, Cambridge, MA 02138; [b]Department of Atmospheric Science, Colorado State University, Fort Collins, CO 80523; [c]Department of Geophysical Sciences, The University of Chicago, Chicago, IL 60637; and [d]School of Engineering and Applied Sciences, Harvard University, Cambridge, MA 02138

Edited by Mark H. Thiemens, University of California, San Diego, La Jolla, CA, and approved June 19, 2014 (received for review April 24, 2014)

The effect of clouds on climate remains the largest uncertainty in climate change predictions, due to the inability of global climate models (GCMs) to resolve essential small-scale cloud and convection processes. We compare preindustrial and quadrupled CO_2 simulations between a conventional GCM in which convection is parameterized and a "superparameterized" model in which convection is explicitly simulated with a cloud-permitting model in each grid cell. We find that the global responses of the two models to increased CO_2 are broadly similar: both simulate ice-free Arctic summers, wintertime Arctic convection, and enhanced Madden–Julian oscillation (MJO) activity. Superparameterization produces significant differences at both CO_2 levels, including greater Arctic cloud cover, further reduced sea ice area at high CO_2, and a stronger increase with CO_2 of the MJO.

global warming | climate sensitivity | climate projections

Clouds play an important role in the climate system by reflecting incoming shortwave solar radiation (cooling), intercepting outgoing longwave radiation from the surface (warming), and influencing temperature and circulation. Their net radiative impact at the surface is about –20 W/m^2 cooling in the global mean, and regional impacts can approach ~40 W/m^2. Understanding how clouds will respond to rising CO_2 concentrations is thus a critical issue in climate science. Progress has been complicated by the hundred-kilometer horizontal grid spacing of most global circulation models (GCMs), which remain unable to directly resolve the much smaller-scale turbulent motions involved in atmospheric moist convection, the corresponding cloud-formation processes, and their radiative effects (1, 2).

Current treatment of convection in global climate models relies on parameterizations and therefore suffers significant uncertainties, particularly relating to the representation of convection and clouds in a changing climate. Model results are sensitive to formulation and parameter choices in parameterized convection schemes. As a result, the magnitude of cloud feedbacks remains uncertain and inconsistently predicted by different models (2). An alternative approach, "superparameterization," attempts to reduce the uncertainties of parameterization by running a higher resolution cloud-permitting model in a small domain within each grid cell of the atmospheric GCM, simulating the convection and cloud motions more explicitly (3, 4). Superparameterized GCMs have been shown to have a more realistic representation of convective variability, including the diurnal cycle (5) and intraseasonal variability such as the Madden–Julian oscillation (MJO) (6) and the Australian and Indian monsoons. They are beginning to be used to project future climate changes (7), although such work has been limited due to computational costs of about 100 times that of a standard GCM.

Here we present the results of running a global coupled ocean–atmosphere model [the Community Earth System Model (CESM; ref. 8)], and its superparameterized variant (SP-CESM; refs. 3, 4, 9) at a preindustrial CO_2 concentration, as well as at 4 times higher concentration. We run CESM to near steady state for both preindustrial CO_2 concentration and 4 times this value ($\times1CO_2$ and $\times4CO_2$), and then run shorter simulations of SP-CESM starting from these steady states (*Materials and Methods*). We choose to examine a rather significant (although not necessarily unrealistic) $\times4CO_2$ increase scenario because the equilibrium climate sensitivity of CESM to CO_2 doubling is on the low side of the warming range of 2.1–4.7 K seen in a recent model intercomparison (10), and to maximize the signal-to-noise ratio in the model response to superparameterization.

CESM and SP-CESM are nearly identical except for their convection and cloud representation and related physics (*Materials and Methods*), but they show significant differences in their simulations at $\times1$ and $\times4CO_2$. Concerns have been raised that convection and cloud parameterizations may lead to either artificial amplification or weakening of the response to CO_2 increase. We find the global climate responses of CESM and SP-CESM to be broadly similar, a reassuring result in terms of present projections that are based on parameterized models. However, we find significant regional differences for Arctic sea ice and the tropical Madden–Julian oscillation on which we focus in this paper. Specifically, we find that SP-CESM shows (*i*) significantly less sea ice at $\times1CO_2$ and a larger area reduction at $\times4CO_2$, and (*ii*) a stronger MJO at $\times1CO_2$ and a larger increase at $\times4CO_2$. We analyze these differences and discuss the implications for uncertainties in climate change projections.

The Arctic, and Arctic sea ice melting in particular, is strongly affected by the presence of low clouds that reduce solar heating in summer and by high clouds that induce warming in winter. Arctic sea ice has undergone rapid recent changes (11, 12), and is believed to have played a major role in past abrupt climate changes (13). Sea ice has a major impact on climate due to its high albedo and ability to insulate the atmosphere from the

Significance

The representation of clouds and convection has an enormous impact on simulation of the climate system. This study addresses concerns that conventional parameterizations may bias the response of climate models to increased greenhouse gases. The broadly similar response of two models with parameterized and nonparameterized convection and clouds suggests that state-of-the-art predictions, based on parameterized climate models, may not necessarily be strongly biased in either direction (too strong or too weak warming). At the same time, large differences in simulated tropical variability and Arctic sea ice area suggest that improvement in convection and cloud representations remains essential.

Author contributions: N.P.A., D.A.R., and E.T. designed research; N.P.A., M.B., M.A.B., D.S.A., Z.K., D.A.R., and E.T. performed research; and N.P.A., D.S.A., Z.K., D.A.R., and E.T. wrote the paper.

The authors declare no conflict of interest.

This article is a PNAS Direct Submission.

Freely available online through the PNAS open access option.

[1]Present address: Department of Atmospheric Science, Colorado State University, Fort Collins, CO 80523.

[2]To whom correspondence may be addressed. Email: eli@eps.harvard.edu, nathan@atmos.colostate.edu, or randall@atmos.colostate.edu.

This article contains supporting information online at www.pnas.org/lookup/suppl/doi:10.1073/pnas.1407175111/-/DCSupplemental.

EARTH, ATMOSPHERIC, AND PLANETARY SCIENCES warmer ocean. Arctic sea ice change impacts local ecosystems (14), modulates extreme weather events in the sub-Arctic and midlatitudes (15), and has implications for shipping routes (16).

Our focus on the MJO is motivated in part by numerous studies showing that present-day MJO simulations with SP-CESM are significantly improved relative to results from conventional GCMs, which have historically struggled to simulate it realistically. The MJO is characterized by an envelope of convective anomalies with a 30–70-day timescale that forms episodically over the Indian Ocean, propagates slowly eastward at around 5 m/s, and dissipates over the central Pacific (17, 18). The MJO affects the monsoons and Atlantic tropical cyclogenesis, modulates westerly wind bursts that can help trigger El Niño events, dramatically impacts tropical rainfall, and contributes to extreme precipitation events globally (18, 19). There is observational (20–23) and model (24–27) evidence of enhanced MJO activity with warming, although not all models agree on the sign of MJO change (28), and the change may be sensitive to the spatial pattern of warming (29).

Results

Arctic Response and Wintertime Convection. The $\times 1CO_2$ control runs for both models show wintertime maximum ice extent that is comparable to observations (1978–1987, Hadley Centre sea ice and sea surface temperature dataset), although with excess sea ice around Greenland. The summertime ice area is smaller than observed in SP-CESM and larger in CESM (Fig. S1). Sea ice thickness is greater than observed in CESM, although it is smaller than observed yet closer to observations in SP-CESM in all seasons (1978–1987, pan-Arctic ice ocean modeling and assimilation system; ref. 30).

To understand the sea ice differences at $\times 1CO_2$ (Fig. 1 and Fig. S1), we first examined the atmospheric meridional heat flux into the Arctic (eddy and mean, dry and moist), but found poleward fluxes in SP-CESM were actually weaker than in CESM. The short length of the SP-CESM simulations further suggests that changes in ocean dynamics are unlikely to contribute to the difference in sea ice, although changes to ocean convection patterns are found in the North Atlantic. This leaves local atmospheric effects, which may be a direct consequence of the different atmospheric convection representation, to explain SP-CESM's reduced sea ice. Indeed, we find larger downward longwave (LW) radiation at the surface in the SP-CESM simulation, with an Arctic average of 11 W/m^2 (Fig. 1*B*). Roughly half of this difference is associated with a systematically larger cloud fraction in SP-CESM (Fig. 1*D*) and the remainder with clear-sky effects (Fig. 1*C*) including a warmer and moister lower troposphere (Fig. 1 *E* and *F*). The larger SP-CESM downward LW radiation at $\times 1CO_2$ occurs most significantly over areas where ocean was exposed by melting sea ice relative to CESM, indicating a feedback via increased evaporation, clouds, and downward LW radiation. However, such enhancement is also seen over Arctic areas covered by sea ice in both models and far from open ocean. Although one cannot rule out enhanced moisture advection in SP-CESM into these ice-covered areas, the very different treatment of clouds and convection in SP-CESM may be responsible for these changes, and therefore for the different sea ice extent as well. The composition of Arctic clouds differs significantly between the models, with SP-CESM showing a preference for ice-phase clouds relative to CESM. Although both models use essentially the same microphysics scheme, in SP-CESM it is applied on a much finer grid (*Materials and Methods*), possibly accounting for these cloud

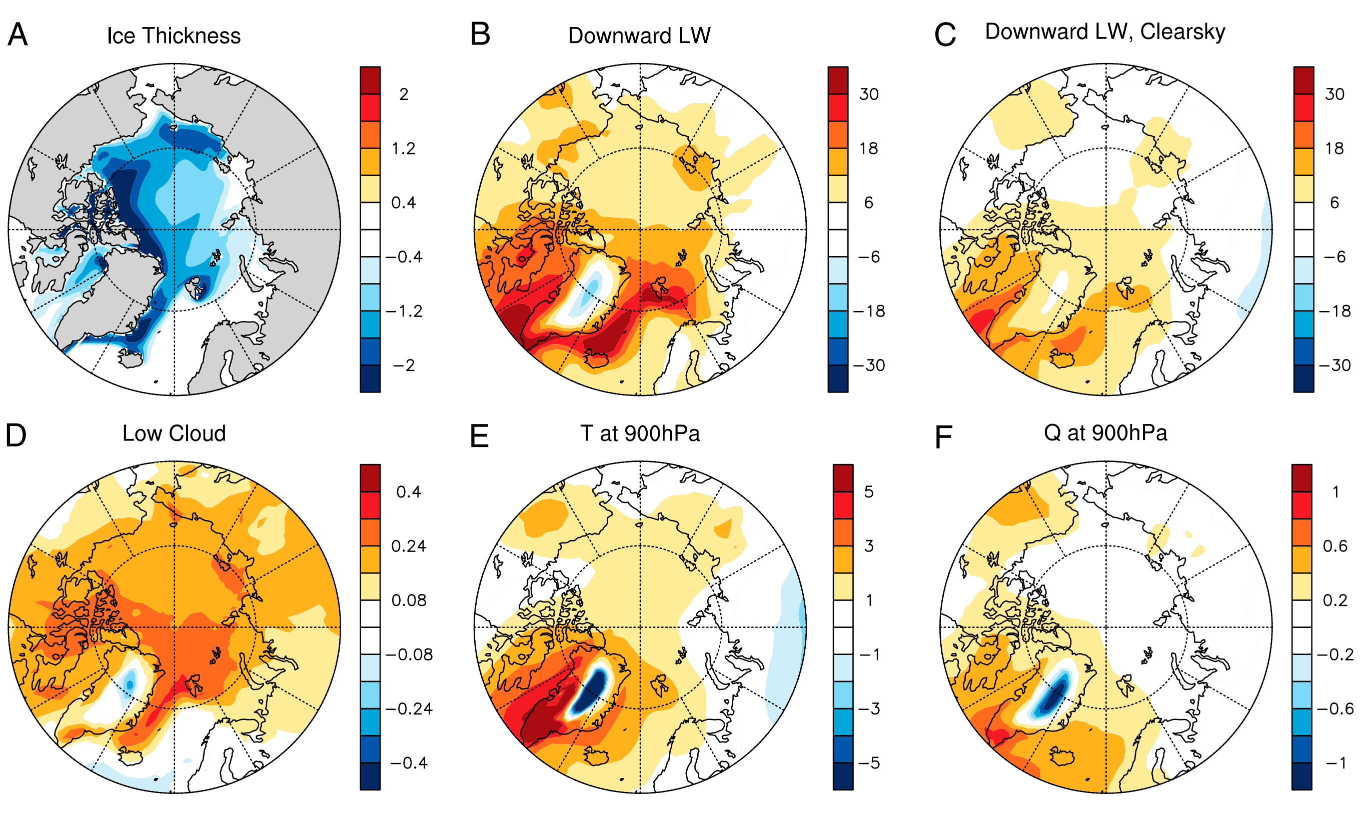

Fig. 1. Understanding the Arctic differences at $\times 1CO_2$ between a model with a more explicit convection representation (SP-CESM) and a model with parameterized convection (CESM). Annual-mean differences, SP-CESM minus CESM, in (*A*) sea ice thickness (in meters), (*B*) downwelling longwave radiation at the surface (W/m^2), (*C*) clear sky downwelling longwave radiation at surface (W/m^2), (*D*) low cloud fraction, (*E*) 900-hPa temperature (in degrees Celsius), and (*F*) 900-hPa specific humidity (in grams per kilogram).

composition differences. We note that annual mean cloud ice content in the SP-CESM control run is somewhat overestimated relative to values derived from CloudSat retrievals (31), whereas those in CESM are closer to observations, suggesting caution in interpreting SP-CESM results.

In response to quadrupled CO_2, the globally averaged surface temperature in CESM increases from 14.5 to 19.3 °C, a climate sensitivity of 2.4 °C per CO_2 doubling. Using the method of ref. 32, this translates to 3.9 °C equilibrium sensitivity. In the SP-CESM runs initialized from CESM, these temperatures decrease at $\times 1CO_2$ and increase slightly at $\times 4CO_2$, to 14.1 and 19.4 °C, respectively. Although these numbers suggest a comparable climate sensitivity, the analysis of ref. 32 suggests that the SP-CESM simulation is not sufficiently close to equilibrium to be able to estimate this model's equilibrium climate sensitivity. The global mean cloud longwave radiative forcing decreases by −1.12 W/m^2 in SP-CESM and −1.45 W/m^2 in CESM, and the shortwave cloud forcing increases by 0.52 W/m^2 in SP-CESM and decreases −0.16 W/m^2 in CESM. In the Arctic, surface temperatures increase by 10.3 and 10.5 °C in CESM and SP-CESM, respectively. Both models become ice free in summer, but retain some winter sea ice cover (Fig. S1). SP-CESM shows a greater reduction in sea ice fraction during the transition months (June, July, December, and January) relative to CESM (Fig. 2 *A* and *E*, and Figs. S1 and S2), and CESM shows larger reductions in ice volume in all months (Figs. S1 and S2). This appears to result from the relative thickness of the multiyear ice in their control runs. Both models lose almost all of their multiyear ice at $\times 4CO_2$, and the first year ice they continue to form is of similar thickness.

Given the strong positive feedbacks due to sea ice melting, and the spread in sea ice ensemble predictions using even a single model (12), we first checked that the stronger response of sea ice area in SP-CESM to increased CO_2 is not merely an amplification of a random perturbation by the positive feedbacks. For this purpose we initialized CESM with the final state of SP-CESM at $\times 4CO_2$ and found that the model immediately went back to its CESM steady state, including a larger sea ice cover (Fig. S3). The difference between the simulation of the two models is clearly larger than the interannual variability of CESM at $\times 4CO_2$. This demonstrates that the two different states found by CESM and SP-CESM at $\times 4CO_2$ indeed reflect systematic differences between the two models, rather than correspond to two ensemble members due to the amplification of random perturbations.

Both models show increases in downward LW radiation at the surface at $\times 4CO_2$, and the increases are particularly large during winter in regions of reduced sea ice fraction (Fig. 2 *B* and *F*). These ice-free regions also develop increased evaporation, water

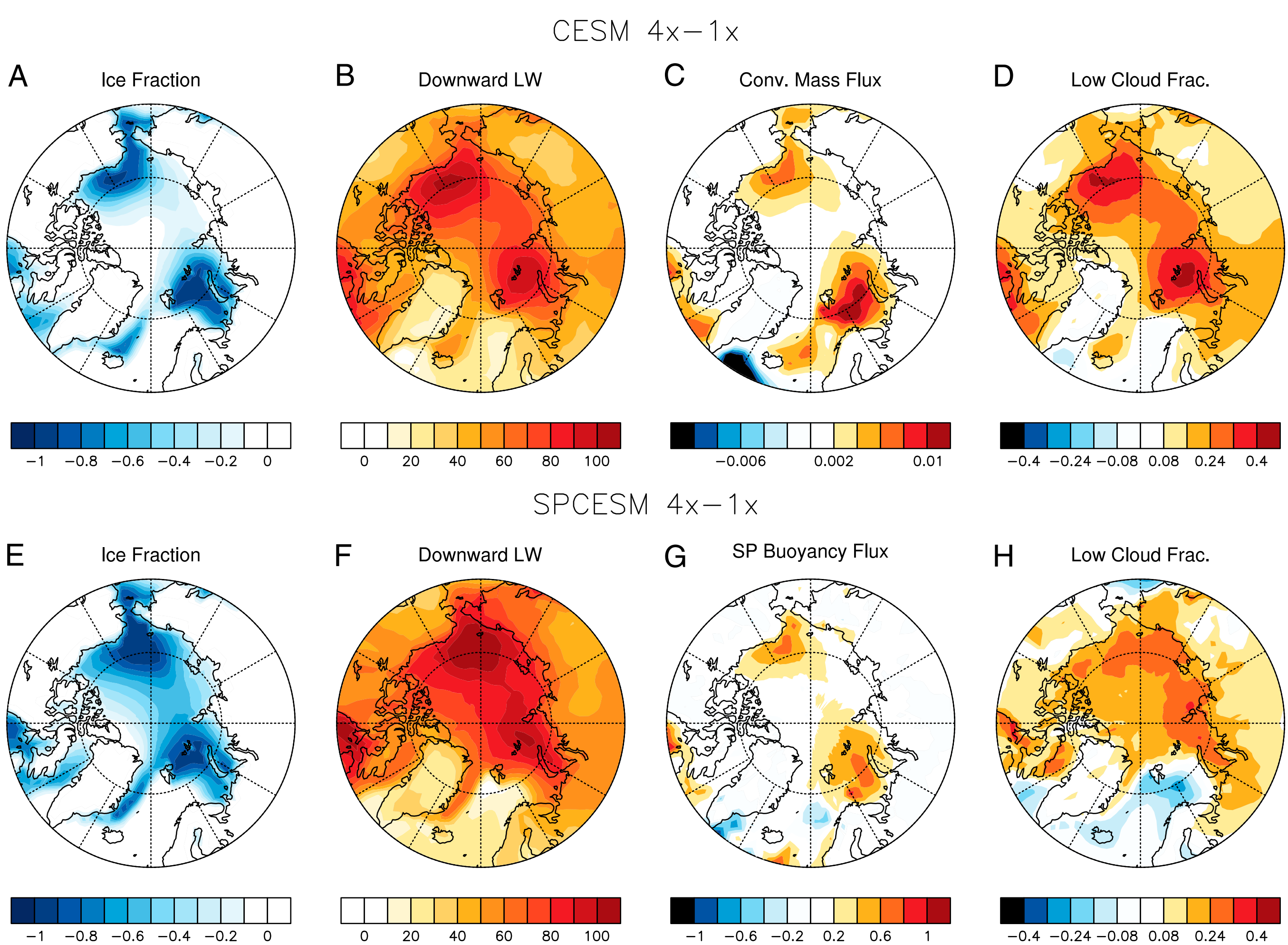

Fig. 2. Comparing the winter (December–February) response to CO_2 increase ($\times 4CO_2 - \times 1CO_2$) for both models. The change in (*A* and *E*) sea ice fraction, (*B* and *F*) downwelling longwave at the surface (W/m^2), (*C*) vertically averaged parameterized convective mass flux (kilograms per second) and (*G*) explicitly simulated buoyancy flux (W/m^2) indicating active convection, and (*D* and *H*) low cloud fraction. SP-CESM shows larger loss of sea ice area but both models exhibit similar changes in downward LW, convection, and cloud fraction.

vapor, shallow wintertime convection, locally increased cloud fraction (Fig. 2 *C, D, G*, and *H*), and consequently also enhanced cloud radiative forcing. (Enhanced shortwave absorption by open ocean in SP-CESM contributes significantly less). Although surprising and seemingly nonintuitive, this convection during polar night in the absence of solar radiation is consistent with the convective cloud feedback recently seen in a hierarchy of climate models with parameterized convection and in reanalysis products (33–35). This wintertime positive cloud feedback is a dramatic result, especially when simulated with the more explicit cloud representation of SP-CESM.

Arctic cloud ice content at low elevations increases more with CO_2 in SP-CESM than in CESM, although cloud liquid increases a bit less at slightly higher elevations (Fig. S4; the stronger SP-CESM response of cloud ice to CO_2 increase is consistent with the fact that SP-CESM has a larger ice cloud concentration at $\times 1CO_2$).

MJO Strengthening. Turning to the effects of the more explicit representation of convection in SP-CESM on the tropics, we first consider the mean climate. At $\times 1CO_2$ both models show significant biases relative to observations, with a pronounced double ITCZ and insufficient equatorial precipitation in CESM, and too much precipitation over the west Indian Ocean and Southeast Asia in SP-CESM. We also find a relative deficit in Southern Ocean shortwave cloud forcing, suggesting that the excess Southern Hemisphere precipitation may be explained by the mechanism of ref. 36. The $\times 4CO_2$ SP-CESM simulation generally shows greater tropical warming than CESM (tropical-mean warming of 4.2 versus 3.6 °C for CESM), particularly in the east Pacific cold tongue region. Mean precipitation increases in both models, but with quite different spatial patterns. CESM maintains a strong double intertropical convergence zone year round, and in SP-CESM precipitation becomes strongly favored in the summer hemisphere (Fig. S5).

Superparameterization has previously been shown to improve simulations of the present-day MJO (6, 37), and we find similar improvements in our simulations at $\times 1CO_2$ (Fig. 3 *A, C, E*, and *G*). The equatorial wavenumber-frequency spectrum for symmetric modes (Fig. 3*E*) shows that CESM variability at $\times 1CO_2$ is much weaker than observed and far from realistic. SP-CESM, on the other hand, shows realistic Kelvin, Rossby, and inertia-gravity wave bands and a strong and nearly realistic MJO peak (Fig. 3*G*; ref. 38), yet it still somewhat underestimates total tropical precipitation variability relative to observations (e.g., National Aeronautics and Space Administration Global Precipitation Climatology Project daily 1° gridded dataset; ref. 39). A composite of outgoing longwave radiation, precipitation, and 850-hPa wind anomalies associated with the MJO closely resembles composites of observations, with similar amplitude, primarily eastward propagation and seasonality.

Proceeding to the response to increased CO_2, we note that several metrics suggest an increase in MJO-like variability in both models as CO_2 is quadrupled, but with particularly large increases in SP-CESM. For example, the SD of daily equatorial (10°S–10°N) precipitation within the MJO band (defined as 20–100 d, zonal wavenumbers 1–3) responds to the increased CO_2 by increasing from 0.45 to 0.7 mm/d in CESM, and from 0.69 to 1.24 mm/d in SP-CESM. In addition, an empirical orthogonal function (EOF)-based MJO index (40) indicates that the two leading modes (associated with the MJO) together account for 28% of intraseasonal variance in CESM at $\times 1CO_2$ (36% at $\times 4CO_2$) and 42% in SP-CESM (52% at $\times 4CO_2$). Thus, the spatially coherent MJO signal accounts for a larger fraction of the larger intraseasonal variance in SP-CESM, with similarly greater increases at high CO_2.

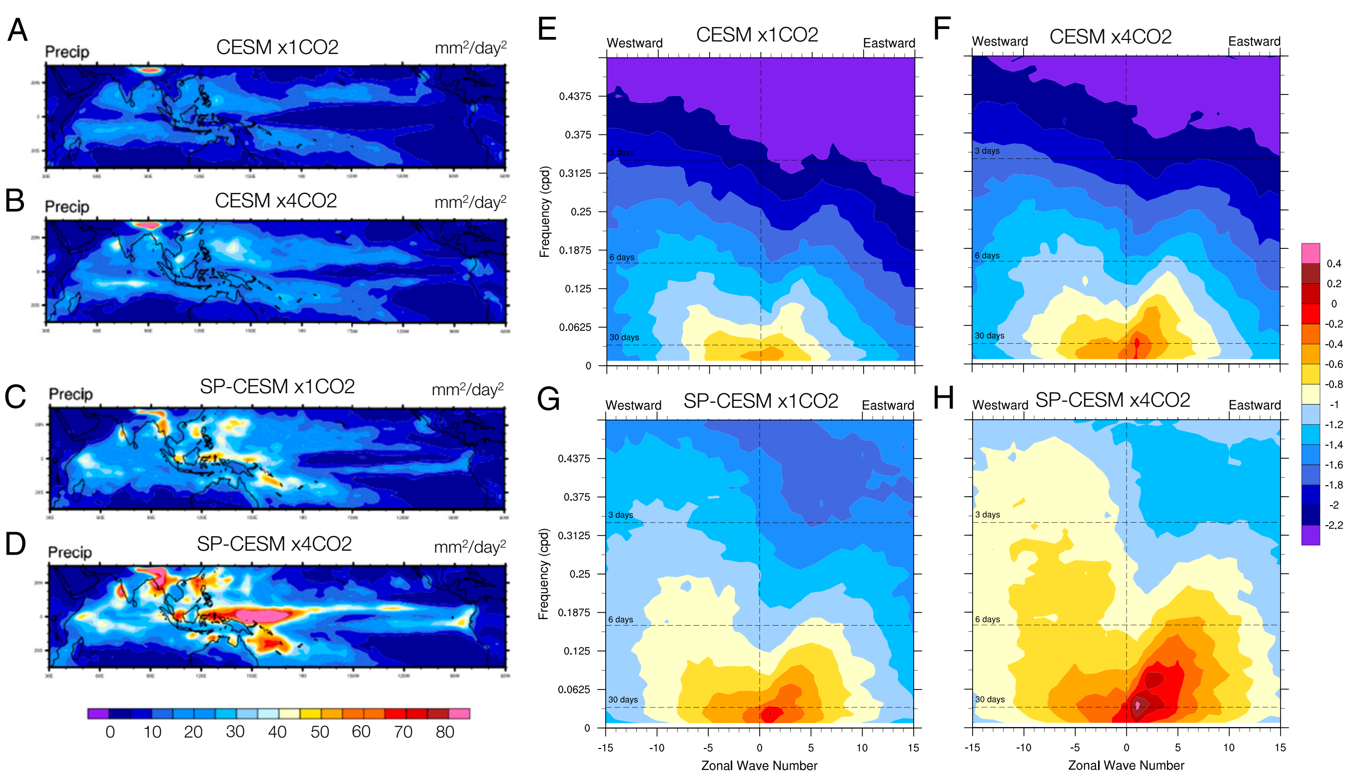

Fig. 3. Exploring the enhanced response of tropical intraseasonal variability in SP-CESM relative to CESM due to stronger increase in MJO in SP-CESM. This is shown via tropical precipitation variability in CESM and SP-CESM. (*A–D*) Annual-mean intraseasonal (20–100 d) variance at low and high CO_2. (*E–H*) Wavenumber-frequency power spectra of equatorial (10°S–10°N) precipitation, for modes that are symmetric across the Equator. SP-CESM simulates more realistic intraseasonal variance at $1\times CO_2$, and shows a larger increase with warming.

Although the mechanism of the MJO is still not well understood, it is generally believed to be a "moisture mode" owing its existence to the interaction of convection with variations in humidity (41). A moist static energy (MSE) budget is therefore a useful diagnostic tool (42), and we apply it here to understand the mechanism behind MJO intensification. The column-integrated budget terms, including large-scale MSE advection, surface fluxes, and radiative heating, are calculated by averaging intraseasonal anomalies within active MJO periods identified by the EOF-based index cited above. The contribution F_ϕ from each budget term to the growth of MSE anomalies is estimated from the vector projection of the composite budget term $\phi(x, y)$ on the composite MSE anomaly $h(x, y)$ given by (43) $F_\phi = \iint \phi \cdot h \, dA / \iint h \cdot h \, dA$. Changes in these contributions with warming suggest changes in physical processes that may explain the stronger MJO activity.

In SP-CESM, the composite MSE budgets show that the MJO at both $\times 1CO_2$ and $\times 4CO_2$ is principally supported by fluctuations in LW radiative heating, which covary with the MSE anomaly (Fig. S6*A*). The budgets also indicate positive shifts in vertical advection and surface latent heat fluxes (LH) in response to the CO_2 increase. A decomposition of the vertical advection term into climatological mean, intraseasonal, and residual components indicates that the shift is entirely due to a steeper mean MSE profile in the warmer climate (Fig. S6*B*). The vertical MSE profile is characterized by a midtropospheric minimum associated with the decrease in humidity away from the surface. The Clausius–Clapeyron relationship then implies that the MSE gradient between the midtroposphere and surface will increase with warming. This increase promotes MSE accumulation in regions of anomalous ascent, and MSE export in regions of descent. Because regions of ascent within the MJO are associated with high MSE, and descent with lower MSE, the change in vertical advection provides a positive feedback on MJO growth. This is consistent with the results of a previous study in which SP-community atmospheric model (CAM) was run in an aquaplanet configuration (27).

A similar decomposition of the contribution from surface latent heat flux shows that the flux increases approximately with Clausius–Clapeyron scaling, at 7%/K. However, because the MJO MSE anomalies increase faster than this, the projected forcing due to latent heat fluxes decreases in magnitude. Because the fluxes are out of phase with MSE at $\times 1CO_2$, ($F_{LH} < 0$), the change in magnitude at $\times 4CO_2$ appears as a positive shift, more favorable for MSE growth. We interpret this as a positive feedback on the stronger MJO rather than its primary cause, because the mechanism requires a greatly increased MSE anomaly to begin with.

Unfortunately, the significantly weaker MJO in CESM does not allow the construction of a composite MSE budget for that model, and therefore a direct comparison of budgets between the models is not possible. The amplification mechanism suggested above does not depend on the convection representation, and could account for the relative increase in MJO activity seen in CESM.

An interesting consequence of the stronger increase in MJO variability in SP-CESM is the development of a positive zonal wind anomaly at 100–300 mb in the tropics (Fig. S7, *Center*). This is consistent with a tendency toward superrotation (westerly wind at the Equator) due to enhanced wave excitation at the Equator, and was seen in previous simulations of warm climates (25, 27). Such a tendency was proposed as a possible explanation for the Pliocene (2–5 Mya) "permanent El Niño" state (44) as well as a possible response of a future climate (45, 46). These proposed consequences require a westerly response near the surface and not at high altitude as seen in Fig. S7, *Center*, but it is possible that the addition of convective momentum transport to SP-CESM would lead to some surface effect.

The models used here cannot reliably be used to study the stratospheric climate response due to insufficient resolution there. However, we briefly note that SP-CESM shows a significant lack of wintertime cooling (i.e., warming relative to CESM; Fig. S7, *Right*) in the Arctic stratosphere, although such cooling is a robust expected consequence of greenhouse scenarios. This relative warming is consistent with changes in the eddy momentum flux [$\Delta(\overline{u'v'})$; Fig. S7, *Left*] and stratospheric jet weakening (Fig. S7, *Center*). Future work will examine the robustness of this result and possible connections to momentum fluxes from the stronger tropical variability found above (47).

Discussion

We have performed a focused comparison of two coupled climate models, nearly identical except that one uses an explicit representation of convection and related processes, rather than a convective parameterization. At $\times 1CO_2$, we find the superparameterization produces much greater Arctic cloud coverage and a warmer and wetter Arctic lower troposphere, resulting in stronger downward longwave radiation, and a reduced, closer to observations, sea ice thickness. In the tropics, SP-CESM simulates stronger and more realistic MJO activity, but both models struggle to reproduce observed patterns of precipitation.

Despite their differences and deficiencies, both models respond to increased CO_2 in qualitatively similar ways. These include increases in MJO activity, similar patterns of Arctic sea ice loss, increases in Arctic cloudiness, and the appearance of wintertime convection over ice-free regions as part of a positive convective cloud feedback. The overall similar response of the superparameterized model is reassuring in terms of our understanding of global climate sensitivity based on parameterized models. However, at the same time we find significant sensitivity of important regional climate features in the Arctic and tropics to the treatment of clouds and convection. This sensitivity makes it clear that continued attention must be focused on convection dynamics and new ways of representing it in future climate change studies.

Materials and Methods

We use CESM1_0_2, with CAM4 atmospheric physics. The CAM was configured to run with the finite-volume dynamical core run at 1.9×2.5 degree horizontal resolution with 26 vertical levels. The community land model (CLM) used the same horizontal grid. The parallel ocean program 2 ocean model (48) and the sea ice model were run on the gx1v6 grid, at a nominal resolution of 1°. The CAM and CLM were run using a 15-min time step while the cloud-permitting models are integrated with a 20-s time step. Each CAM grid cell contains a 2D cloud-permitting model (CRM) run in a two-dimension configuration aligned in an east–west direction, with a total of 32 grid points and horizontal grid spacing of 4 km. The CRM of the SP-CESM also replaces the stratiform cloud parameterization of the CESM. Another important difference between the two models is that the radiation and turbulence calculations are done on the CRM's grid in SP-CESM. Finally, although we showed that convection representation can make a significant difference, other cloud-formation processes such as microphysics parameterizations are, of course, also critical, and ice clouds in particular are different with the two-moment microphysics that is included in the recently released CAM5. As another caveat, we note that the Antarctic effective cooling of SP-CESM seen in Fig. S7, *Right* at around 200 mb occurs in a region and altitude where SP-CESM at $\times 1CO_2$ further deviates from the observed (reanalysis) temperature field and is therefore questionable.

CESM runs at increased CO_2 concentration are started from a steady state at $\times 1CO_2$, specifying a 1% increase in CO_2 a year until $\times 4CO_2$ is reached and then integrating 170 additional years until the model equilibrates to a large degree. SP-CESM integrations of 16 and 13 y are then started from the $\times 1$ and $\times 4$ CESM steady states, correspondingly. The figures shown are based on 5-y means at the end of each model run. The main results reported are robust at 5-y mean, even considering interannual model variability.

ACKNOWLEDGMENTS. We thank two anonymous reviewers for their constructive and helpful comments. E.T. thanks the Weizmann Institute for its hospitality during parts of this work. This work was supported by National Science Foundation Grant AGS-1303604 (to E.T. and N.P.A.). D.S.A. was supported by an Alfred P. Sloan research fellowship.

1. Held IM, Soden BJ (2000) Water vapor feedback and global warming. *Annu Rev Energy Environ* 25:441–475.
2. Bony S, et al. (2006) How well do we understand and evaluate climate change feedback processes? *J Clim* 19:3445–3482.
3. Grabowski WW (2001) Coupling cloud processes with the large-scale dynamics using the cloud-resolving convection parameterization (CRCP). *J Atmos Sci* 58:978–997.
4. Randall D, Khairoutdinov M, Arakawa A, Grabowski W (2003) Breaking the cloud parameterization deadlock. *Bull Am Meteorol Soc* 84:1547–1564.
5. Pritchard M, Somerville R (2009) Assessing the diurnal cycle of precipitation in a multi-scale climate model. *J Adv Mod Earth Sys* 1:16.
6. Benedict JJ, Randall DA (2009) Structure of the Madden–Julian oscillation in the superparameterized CAM. *J Atmos Sci* 66:3277–3296.
7. Stan C, Xu L (2014) Climate simulations and projections with the super-parameterized CCSM4. *Environ Model Softw* 60:134–152.
8. Gent PR, et al. (2011) The Community Climate System Model version 4. *J Clim* 24: 4973–4991.
9. Stan C, et al. (2010) An ocean-atmosphere climate simulation with an embedded cloud resolving model. *Geophys Res Lett* 37:L01702.
10. Andrews T, Gregory JM, Webb MJ, Taylor KE (2012) Forcing, feedbacks and climate sensitivity in CMIP5 coupled atmosphere-ocean climate models. *Geophys Res Lett* 39:L09712.
11. Comiso JC, Parkinson CL, Gersten R, Stock L (2008) Accelerated decline in the Arctic sea ice cover. *Geophys Res Lett* 35:L01703.
12. Holland MM, Bitz CM, Tremblay B (2006) Future abrupt reductions in the summer Arctic sea ice. *Geophys Res Lett* 33.
13. Gildor H, Tziperman E (2003) Sea-ice switches and abrupt climate change. *Phil Trans A Math Phys Eng Sci* 361(1810):1935–1942.
14. Grebmeier JM, et al. (2006) A major ecosystem shift in the northern Bering Sea. *Science* 311(5766):1461–1464.
15. Francis J, Vavrus S (2012) Evidence linking arctic amplification to extreme weather in mid-latitudes. *Geophys Res Lett* 39.
16. Smith LC, Stephenson SR (2013) New Trans-Arctic shipping routes navigable by midcentury. *Proc Natl Acad Sci USA* 110(13):E1191–E1195.
17. Madden RA, Julian PR (1971) Detection of a 40-50 day oscillation in zonal wind in tropical Pacific. *J Atmos Sci* 28:702–708.
18. Zhang C (2005) Madden-Julian oscillation. *Rev Geophys* 43:1–36.
19. Jones C, Waliser DE, Lau K, Stern W (2004) Global occurrences of extreme precipitation and the Madden-Julian Oscillation: Observations and predictability. *J Clim* 17:4575–4589.
20. Slingo J, Rowell D, Sperber K, Nortley E (1999) On the predictability of the interannual behaviour of the Madden-Julian oscillation and its relationship with El Niño. *Q J R Meteorol Soc* 125:583–609.
21. Hendon HH, Zhang C, Glick JD (1999) Interannual variation of the Madden–Julian Oscillation during austral summer. *J Clim* 12:2538–2550.
22. Jones C, Carvalho LMV (2006) Changes in the activity of the Madden–Julian Oscillation during 1958–2004. *J Clim* 19:6353–6370.
23. Oliver EC, Thompson KR (2012) A reconstruction of Madden–Julian Oscillation variability from 1905 to 2008. *J Clim* 25:1996–2019.
24. Lee S (1999) Why are the climatological zonal winds easterly in the equatorial upper troposphere? *J Atmos Sci* 56:1353–1363.
25. Caballero R, Huber M (2010) Spontaneous transition to superrotation in warm climates simulated by CAM3. *Geophys Res Lett* 37:1–5.
26. Schubert JJ, Stevens B, Crueger T (2013) Madden-Julian Oscillation as simulated by the MPI Earth system model: Over the last and into the next millennium. *J Adv Model Earth Syst* 5:71–84.
27. Arnold N, Kuang Z, Tziperman E (2013) Enhanced MJO-like variability at high SST. *J Clim* 26:988–1001.
28. Takahashi C, Sato N, Seiki A, Yoneyama K, Shirooka R (2011) Projected future change of MJO and its extratropical teleconnection in east Asia during the northern winter simulated in IPCC AR4 models. *SOLA* 7:201–204.
29. Maloney ED, Xie SP (2013) Sensitivity of tropical intraseasonal variability to the pattern of climate warming. *J Adv Model Earth Syst* 5:1–16.
30. Zhang J, Rothrock D (2003) Modeling global sea ice with a thickness and enthalpy distribution model in generalized curvilinear coordinates. *Mon Weath Rev* 131: 845–861.
31. Li JLF, et al. An observationally based evaluation of cloud ice water in CMIP3 and CMIP5 GCMs and contemporary reanalysis using contemporary satellite data. *J Geophys Res* 117:D16105.
32. Gregory J, Webb M (2008) Tropospheric adjustment induces a cloud component in CO_2 forcing. *J Clim* 71:58–71.
33. Abbot DS, Tziperman E (2008) Sea ice, high latitude convection, and equable climates. *Geophys Res Lett* 35:L03702.
34. Abbot DS, Walker C, Tziperman E (2009) Can a convective cloud feedback help to eliminate winter sea ice at high CO_2 concentrations? *J Clim* 22:5719–5731.
35. Leibowicz BD, Abbot DS, Emanuel KA, Tziperman E (2012) Correlation between present-day model simulation of Arctic cloud radiative forcing and sea ice consistent with positive winter convective cloud feedback. *J. Adv. Model. Earth Syst.* 4.
36. Hwang YT, Frierson DMW (2013) Link between the double-Intertropical Convergence Zone problem and cloud biases over the Southern Ocean. *Proc Natl Acad Sci USA* 110(13):4935–4940.
37. Thayer-Calder K, Randall DA (2009) The role of convective moistening in the Madden–Julian Oscillation. *J Atmos Sci* 66:3297–3312.
38. Wheeler M, Kiladis GN (1999) Convectively coupled equatorial waves: Analysis of clouds and temperature in the wavenumber-frequency domain. *J Atmos Sci* 56: 374–399.
39. Huffman G, et al. (2001) Global precipitation at one-degree daily resolution from multi-satellite observations. *J Hydrometeorol* 2:36–50.
40. Wheeler MC, Hendon HH (2004) An all-season real-time multivariate MJO index: Development of an index for monitoring and prediction. *Mon Wea Rev* 132: 1917–1932.
41. Raymond DJ, Fuchs V (2009) Moisture modes and the Madden–Julian Oscillation. *J Clim* 22:3031–3046.
42. Maloney ED (2009) The moist static energy budget of a composite tropical intraseasonal oscillation in a climate model. *J Clim* 22:711–729.
43. Andersen JA, Kuang Z (2012) Moist static energy budget of MJO-like disturbances in the atmosphere of a zonally symmetric aquaplanet. *J Atmos Sci*.
44. Tziperman E, Farrell BF (2009) The Pliocene equatorial temperature — Lessons from atmospheric superrotation. *Paleoceanography* 24:PA1101.
45. Held IM (1999) Equatorial superrotation in earth-like atmospheric models, http://www.gfdl.gov/~ih/papers/super.ps. AMS Bernhard Haurwitz Memorial Lecture, 1999.
46. Pierrehumbert RT (2000) Climate change and the tropical Pacific: The sleeping dragon wakes. *Proc Natl Acad Sci USA* 97(4):1355–1358.
47. Taguchi M, Hartmann D (2006) Increased occurrence of stratospheric sudden warmings during El Niño as simulated by WACCM. *J Clim* 19:324–332.
48. Danabasoglu G, et al. (2012) The CCSM4 ocean component. *J Clim* 25:1361–1389.

Supporting Information

Arnold et al. 10.1073/pnas.1407175111

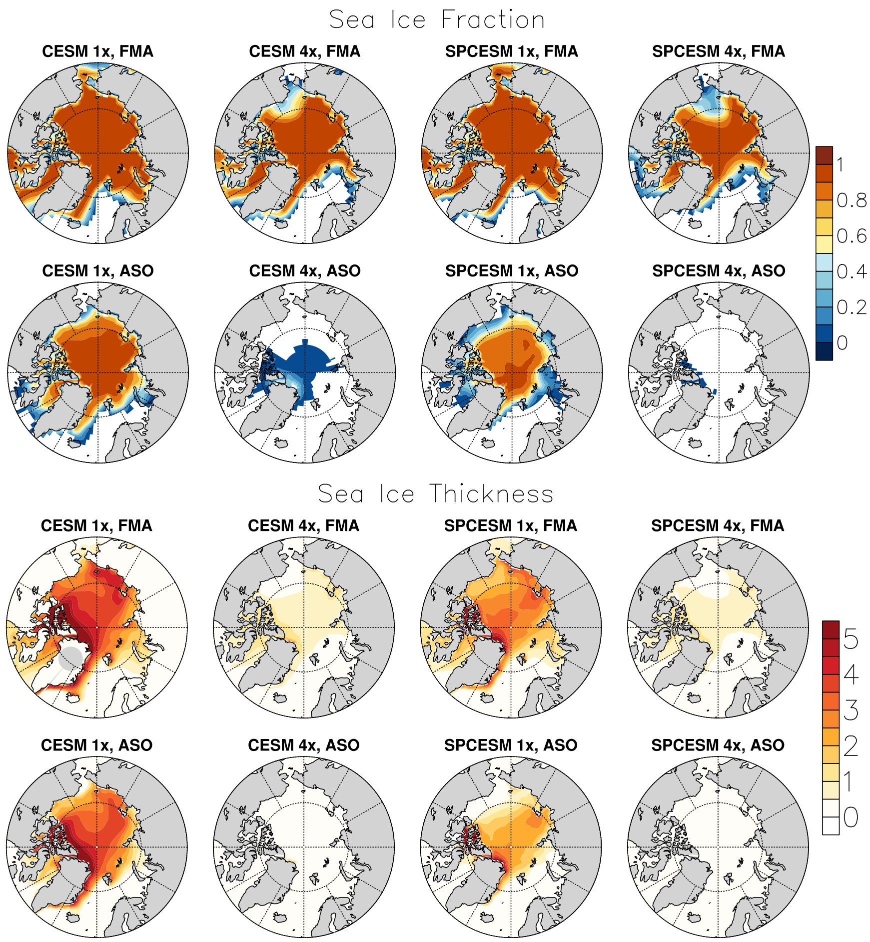

Fig. S1. Arctic sea ice fraction and thickness (in meters) for both models in winter (February–April) and summer (August–October) averaged over 5 y.

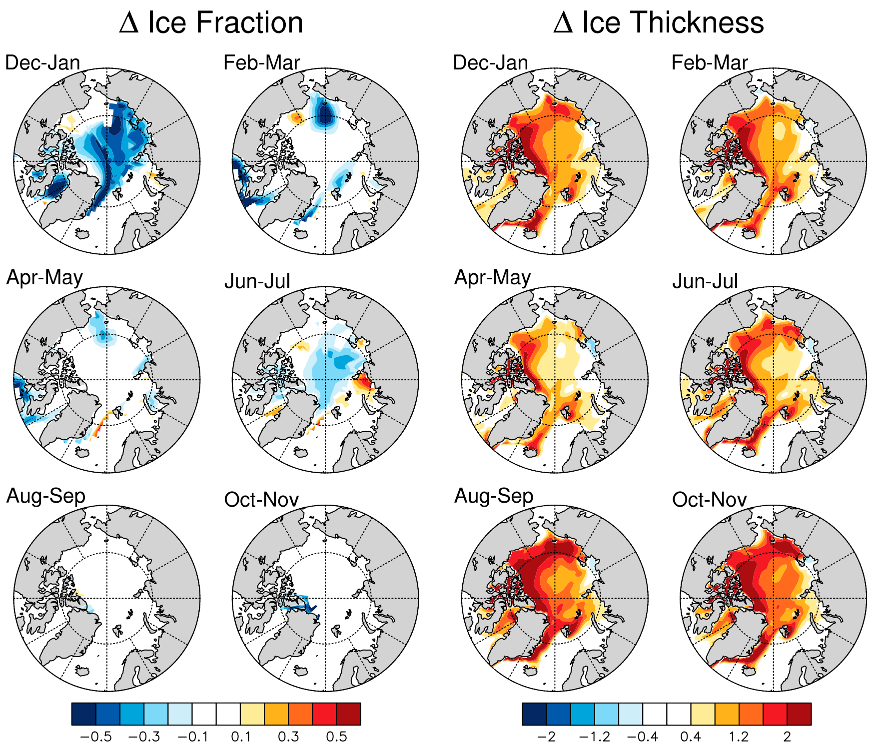

Fig. S2. Difference in response of Arctic sea ice fraction and thickness (meters) between superparameterized Community Earth System Model (SP-CESM) and the Community Earth System Model (CESM; Δ = [SPCESM4×-SPCESM1×]-[CESM4×-CESM1×]) during all months, averaged over 5 y.

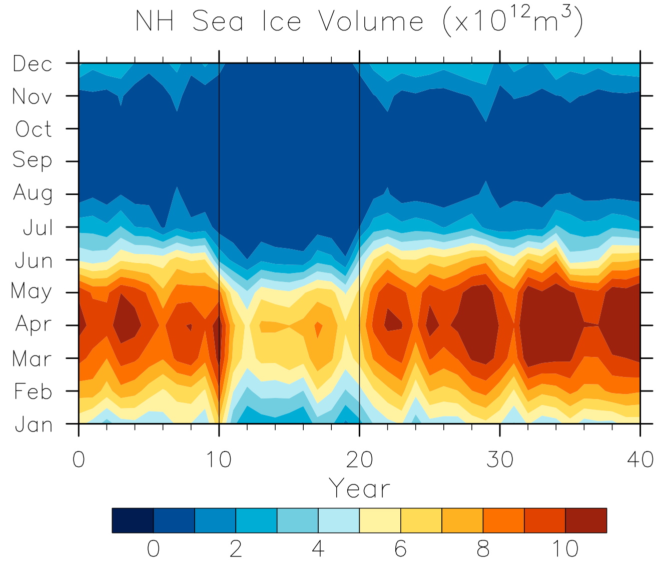

Fig. S3. Arctic sea ice volume as function of month and year during model run. The first 10 y shown are the end of a CESM run to equilibrium. Years 10–20, which show a reduced sea ice volume, are from an SP-CESM that started from the equilibrium CESM solution. Years 20–40 show that sea ice is quickly restored to its higher value when simulated in CESM again, starting from the end state of the SP-CESM run.

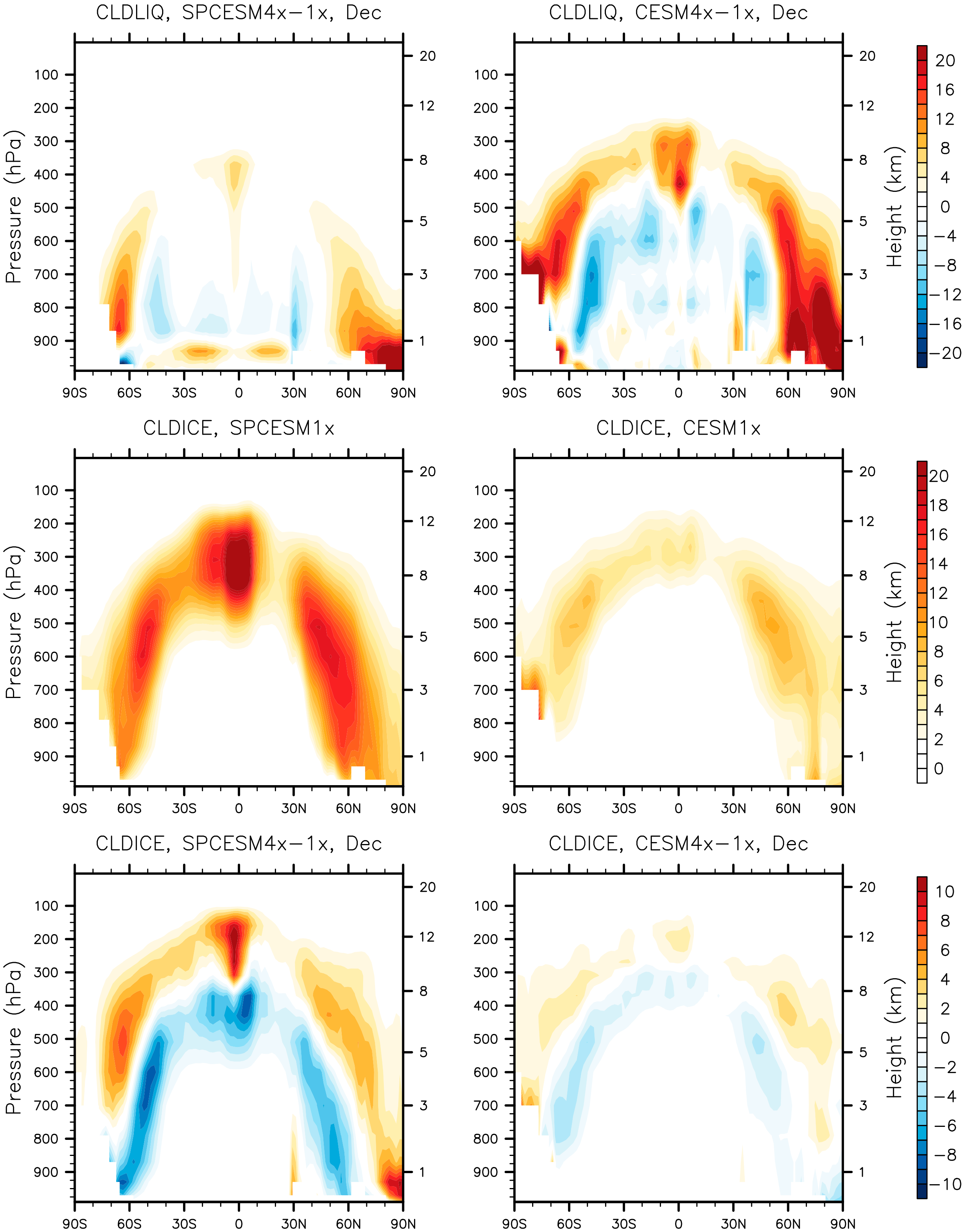

Fig. S4. Cloud ice (grams per kilogram) and cloud water (grams per kilogram) at $\times 1CO_2$ in both CESM and SP-CESM, as well as the difference of $\times 4CO_2$ minus $\times 1CO_2$. SP-CESM has a larger concentration of cloud ice at $\times 1CO_2$, and its cloud response to CO_2 increase is also larger, consistent with the enhanced radiative effects of cloud ice during polar night convection.

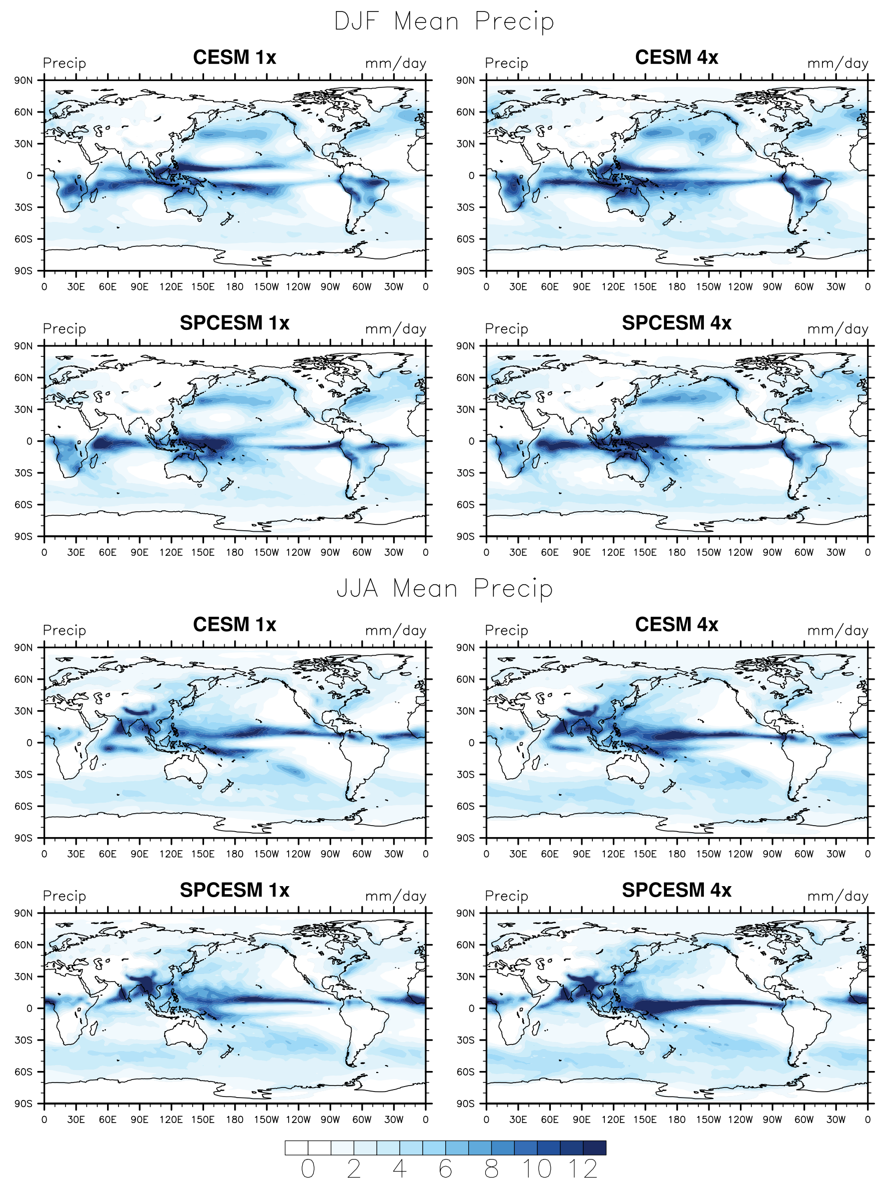

Fig. S5. Mean precipitation in June–August and December–February, for CESM and SP-CESM at ×1 and ×4CO_2. CESM retains a double intertropical convergence zone pattern at ×4CO_2, while SP-CESM shifts to a single rain band (1).

1. Stan C, Xu L (2014) Climate simulations and projections with the super-parameterized CCSM4. *Environ Model Softw*, in press.

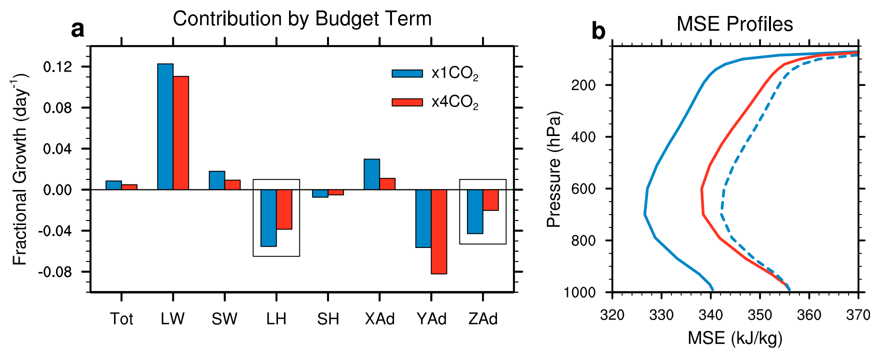

Fig. S6. (*A*) Composite moist static energy (MSE) budget of Madden–Julian oscillation (MJO) variability in SP-CESM. Shown are contributions from each budget term to growth of the MJO MSE anomaly. Positive shifts, in response to CO_2 increase, in vertical advection and latent heat flux can explain the stronger MJO at ×4CO_2. (*B*) Annual-mean MSE vertical profiles over the equatorial (5°S–5°N) Indian and west Pacific Oceans. The ×1CO_2 profile (blue) is also shown shifted (dashed) to allow a direct comparison of the vertical gradients.

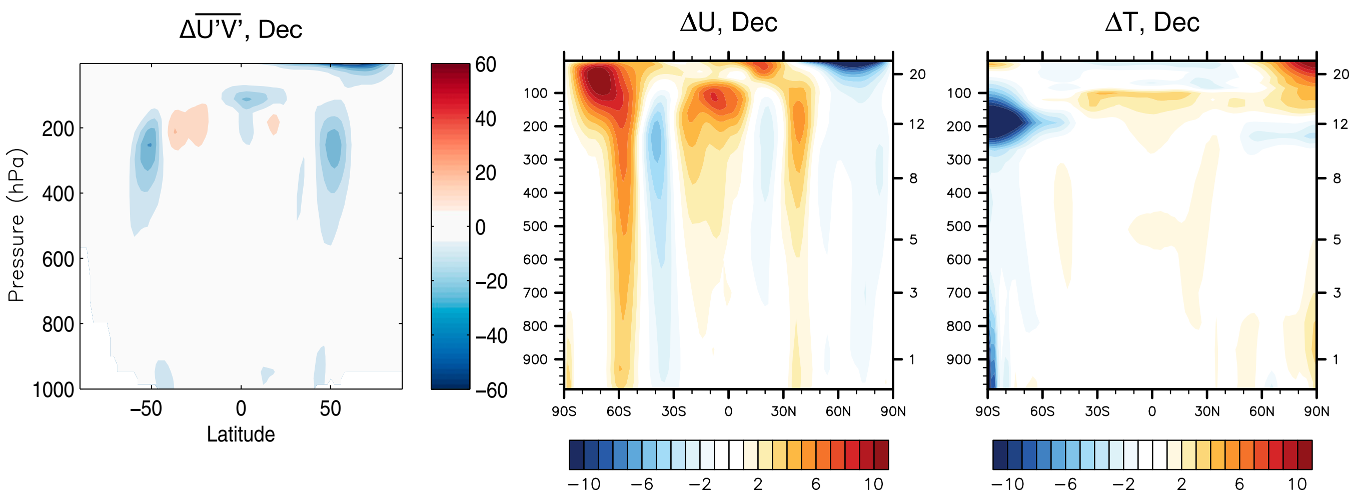

Fig. S7. Differences in zonal-mean response of (*Left*) eddy momentum fluxes (m^2/s^2), showing a contribution in the Arctic stratosphere, (*Center*) zonal wind (m/s), showing equatorial westerly anomalies and weakened Arctic stratospheric jet, and (*Right*) temperature (°C), showing a relative lack of cooling in the SP Arctic stratosphere.